JOURNAL OF AIRCRAFT
Vol. 37, No. 5, September–October 2000

Transonic Flutter Simulations Using an Implicit Aeroelastic Solver

Raymond E. Gordnier* and Reid B. Melville†
U.S. Air Force Research Laboratory, Wright–Patterson Air Force Base, Ohio 45433-7913

Flutter computations are presented for the AGARD 445.6 standard aeroelastic wing configuration using a fully implicit, aeroelastic Navier–Stokes solver coupled to a general, linear, second-order structural solver. This solution technique realizes implicit coupling between the fluids and structures using a subiteration approach. Results are presented for two Mach numbers, $M_\infty = 0.96$ and 1.141. The computed flutter predictions are compared with experimental data and with previous Navier–Stokes computations for the same case. Predictions of the flutter point for the $M_\infty = 0.96$ case agree well with experimental data. At the higher Mach number, $M_\infty = 1.141$, the present computations overpredict the flutter point but are consistent with other computations for the same case. The sensitivity of computed solutions to grid resolution, the number of modes used in the structural solver, and transition location is investigated. A comparison of computations using a standard second-order accurate central-difference scheme and a third-order upwind-biased scheme is also made.

Introduction

AEROELASTICITY is the interaction between a flexible structure and the flow that surrounds it. All flight vehicles are subject to aeroelastic effects, and for many, their performance is limited by adverse aeroelastic interactions. Future aircraft design would benefit from a more comprehensive integration of both positive and negative aeroelastic effects. Aeroelastic simulation promises to be a more timely and cost effective method of achieving this than wind-tunnel or flight testing. The challenge becomes one of developing a robust, affordable, and accurate computational aeroelasticity capability.

Over the past 20 years, great advances have been made in the ability to model accurately and efficiently aerodynamic flows by computing the Euler or Navier–Stokes equations. Recently, a number of researchers have coupled three-dimensional Euler/Navier–Stokes solvers with structural models[1–5] to perform both static and dynamic aeroelastic simulations. All of these examples use a closely coupled but lagged strategy where the fluid and structure equations are solved sequentially. However, this method is limited to first-order accuracy in time due to the lagged coupling regardless of the temporal accuracy of the individual solvers. This type of scheme may also lead to the spurious growth of disturbances in the fluid/structures system due to the effects of the time lag introduced between the fluids and structural solvers.[6] Overcoming this limitation requires implicit coupling, or synchronization, of the two solvers.

A recently developed scheme by Melville et al.,[7] which uses implicit solvers for the fluids and structures, achieves implicit coupling between the fluids and structures via subiterations. Other known benefits of subiterations include the reduction of linearization and factorization errors, synchronization of lagged boundary conditions and turbulence models, and implicit communication between explicitly linked zones in an overset grid or parallel environment. The flow solver in this scheme is a three-dimensional Beam–Warming algorithm.[8] It has been used extensively to simulate a wide range of unsteady flowfields.[9–12] Melville et al.[7] and Morton et al.[13] have extended the functionality of this code to include second-order temporal accuracy, grid deformation capability, application of the geometric conservation law,[14] and a general, linear, second-order structural solver. The technique has also been developed to provide fully implicit results in an overset grid environment and on parallel platforms.[15]

The purpose of the present work is to apply this scheme to the solution of the AGARD 445.6 aeroelastic wing test case.[16] Two cases will be computed, $M_\infty = 0.96$ and 1.141. Comparisons are made with experimental measurements, as well as other computations for the same conditions.[3,4] The sensitivity of the solutions to grid resolution, number of structural modes used, flow solver, that is, a Roe upwind-biased scheme vs central differencing with added dissipation, and transition location will also be investigated.

Governing Equations

Aerodynamic Governing Equations

The aerodynamic governing equations are the unsteady, compressible, three-dimensional Navier–Stokes equations written in nondimensional, strong-conservation law form[17] employing a general time-dependent transformation. The resulting system of governing equations is expressed as

$$\frac{\partial \hat{U}}{\partial t} + \frac{\partial}{\partial \xi}\left(\hat{F} - \frac{1}{Re}\hat{F}_v\right) + \frac{\partial}{\partial \eta}\left(\hat{G} - \frac{1}{Re}\hat{G}_v\right) + \frac{\partial}{\partial \zeta}\left(\hat{H} - \frac{1}{Re}\hat{H}_v\right) = S_{\mathrm{GCL}} \tag{1}$$

With this formulation, the vector of dependent variables $\hat{U}$ is given as

$$\hat{U} = (1/J)U = (1/J)[\rho \quad \rho u \quad \rho v \quad \rho w \quad \rho E]^T \tag{2}$$

All variables have been normalized by the appropriate combination of freestream density, velocity, and a characteristic length. Sutherland's law for the molecular viscosity coefficient μ and the perfect gas relationship are also employed, and Stokes' hypothesis for the bulk viscosity coefficient is assumed.

The source vector term S_{GCL} is a term that arises in the strong conservation law form for moving meshes. This term is defined[13] as

$$S_{\mathrm{GCL}} = U\left[\frac{\partial J^{-1}}{\partial t} + \left(\frac{\xi_t}{J}\right)_\xi + \left(\frac{\eta_t}{J}\right)_\eta + \left(\frac{\zeta_t}{J}\right)_\zeta\right] \tag{3}$$

This term vanishes analytically (geometric conservation law[14]), but not when discrete representations of the temporal and spatial derivatives are used. The most straightforward approach of accounting for

Presented as Paper 98-1729 at the AIAA/ASME/ASCE/AHS/ASC 39th Structures, Structural Dynamics, and Materials Conference and Exhibit, Long Beach, CA, 20–23 April 1998; received 15 September 1998; revision received 30 September 1999; accepted for publication 15 November 1999.

*Research Aerospace Engineer, Computational Sciences Branch. Associate Fellow AIAA.

†Research Aerospace Engineer, Computational Sciences Branch. Senior Member AIAA.

this term is to simply include it in the discrete governing equations, more accurately representing the nontransformed governing equations.

Structural Dynamic Governing Equations

In general the second-order, linear structural equations coupled with the aerodynamic flow solver can be expressed as

$$M\ddot{q} + D\dot{q} + Kq = \Phi^T F_a \tag{4}$$

where q, M, D, and K are displacement, mass, damping, and stiffness. $\boldsymbol{F}_a$ is the vector of aerodynamic forces, and Φ^T is the transformation that maps these forces into the structural system. This equation can be written as a first-order system by defining $S = [q \quad \dot{q}]^T$:

$$\begin{bmatrix} I & 0 \\ 0 & M \end{bmatrix} \dot{S} + \begin{bmatrix} 0 & -I \\ K & D \end{bmatrix} S = \begin{bmatrix} 0 \\ \Phi^T \boldsymbol{F}_a \end{bmatrix} \tag{5}$$

Numerical Procedure

Solutions to Eq. (1) are obtained numerically using the implicit approximately factored finite difference algorithm of Beam and Warming,[8] employing a Newton-like subiteration procedure.[18] The numerical algorithm is obtained from Eq. (1) by utilizing either a two- or three-point backward time differencing and linearizing about the solution at subiteration level p. First- or second-order temporal accuracy is obtained in this iterative approach by specifying either $\phi = 0$ or $\phi = \frac{1}{2}$, respectively, in Eq. (6). The numerical algorithm is written in approximately factored, delta form as

$$\begin{aligned}
&\left[J^{-1^p} + \phi^i \Delta t_s \delta_\xi \left(\frac{\partial F^p}{\partial U} - \frac{1}{Re} \frac{\partial F_v^p}{\partial U} \right) \right] \\
&\times \left[J^{-1^p} + \phi^i \Delta t_s \delta_\eta \left(\frac{\partial G^p}{\partial U} - \frac{1}{Re} \frac{\partial G_v^p}{\partial U} \right) \right] \\
&\times \left[J^{-1^p} + \phi^i \Delta t_s \delta_\zeta \left(\frac{\partial H^p}{\partial U} - \frac{1}{Re} \frac{\partial H_v^p}{\partial U} \right) \right] \Delta U \\
&= -\phi^i \Delta t_s \left\{ J^{-1^p} \frac{(1+\phi)U^p - (1+2\phi)U^n + \phi U^{n-1}}{\Delta t} \right. \\
&- U^p \left[\left(\frac{\xi_t}{J} \right)_\xi + \left(\frac{\eta_t}{J} \right)_\eta + \left(\frac{\zeta_t}{J} \right)_\zeta \right]^p \\
&+ J^{-1^p} \delta_\xi \left(F^p - \frac{1}{Re} F_v^p \right) + J^{-1^p} \delta_\eta \left(G^p - \frac{1}{Re} G_v^p \right) \\
&\left. + J^{-1^p} \delta_\zeta \left(G^p - \frac{1}{Re} G_v^p \right) \right\}
\end{aligned} \tag{6}$$

where

$$\phi^i = 1/(1+\phi), \qquad \Delta U = U^{p+1} - U^p \tag{7}$$

and for $p = 1$, then $U^p = U^n$.

Here U^p is the subiteration approximation to U^{n+1} so that as $p \to \infty$, then $U^p \to U^{n+1}$. Note that with this subiteration approach the right-hand side of Eq. (6) represents the numerical approximation to the governing equation, whereas the left-hand side vanishes as $p \to \infty$. The left-hand side, then, may be modified without loss of formal accuracy provided a sufficient number of subiterates is employed. In particular, a time step on the left-hand side of the equation, Δt_s, may be chosen independently from the physical time step Δt on the right-hand side, thereby enhancing stability. Furthermore, the right-hand side of Eq. (6) can be modified to include a higher-order, upwind-biased algorithm [Roe scheme (see Ref. 19)], lagged boundary conditions or lagged k–ϵ turbulence modeling without destroying the implicit nature of the algorithm.

Left-hand-side efficiency improvements can also be implemented. The numerical procedure has been modified to include diagonalization, following the approach of Ref. 20. Although the diagonalized form of the alternating direction implicit scheme is only first-order time accurate, when coupled with subiterations, higher-order time accuracy may be recovered.[13] The numerical scheme reverts to the standard first-order Beam–Warming procedure for $\phi = 0$, $\Delta t_s = \Delta t$, and $p = 1$.

In Eq. (6), all spatial derivatives are approximated by second-order accurate central differences, and common forms of both implicit and explicit nonlinear dissipation[21] are employed to preserve numerical stability. The temporal metric derivatives are discretized in a manner consistent with the temporal derivative of the conserved variables in Eq. (6).

The subiteration formulation can also be applied to the structural equations [Eq. (5)]. The resulting scheme is

$$\begin{aligned}
\begin{bmatrix} \gamma I & -I \\ K & \gamma M + D \end{bmatrix} \Delta S^p &= \begin{bmatrix} 0 \\ \Phi^T F_a^p \end{bmatrix} - \begin{bmatrix} 0 & -I \\ K & D \end{bmatrix} S^p \\
&- \begin{bmatrix} I & 0 \\ 0 & M \end{bmatrix} \frac{(1+\phi)S^p - (1+2\phi)S^n + \phi S^{n-1}}{\Delta t}
\end{aligned} \tag{8}$$

where $\gamma = (1+\phi)/\Delta t_s$. Because the structural equations are also cast in an iterative form, as $p \to \infty$ a fully implicit coupling between the aerodynamic model and the structural model is obtained.

Grid Deformation Approach

The grid deformation scheme employed was developed in Ref. 7. This algebraic method maintains the grid quality of the initial mesh near deforming surfaces under arbitrary, moderate deflections and rotations. In addition, a specified region in the far field may be held fixed. This is advantageous when this deformation scheme is used in an overset grid context because the grid overlap regions, and their connectivities, will remain unchanged.

Given a starting grid $\hat{x}$ and a surface displacement (assumed to be at $k = 1$ here), the translation and rotation of each surface node is computed from the deflected aerodynamic surface $\hat{x}'_{ij1}$. The translational displacements are

$$\Delta \hat{x}_{ij1} = \hat{x}'_{ij1} - \hat{x}_{ij1} \tag{9}$$

whereas the rotational displacement at the node can be found by forming an orthonormal basis for the original surface position and the perturbed surface, respectively,

$$[E] = [\hat{e}_1 \quad \hat{e}_2 \quad \hat{e}_3], \qquad [E'] = [\hat{e}'_1 \quad \hat{e}'_2 \quad \hat{e}'_3] \tag{10}$$

The surface rotation matrix can be defined as

$$[R] = [E'][E]^T \tag{11}$$

Each normal grid line is then moved in a rigid-body way according to the displacement of the surface node to form a reference, displaced grid line defined by

$$\hat{r}_{i,j,k} = \hat{x}_{i,j,k} + \Delta \hat{x}_{ij1} + [R](\hat{x}_{i,j,k} - \hat{x}_{ij1}) \tag{12}$$

The new grid line is constructed by blending the reference grid line and the old grid line. The blending choice is arbitrary but is best done in arclength space rather than in computational space. The arclength for each node is defined,

$$s_{ijk} = \sum_{l=2}^{k} |\hat{x}_{ijl} - \hat{x}_{ijl-1}| \tag{13}$$

where $s_{ij1} = 0$. A cubic blending with zero slope at the endpoints assures both that wall orthogonality is maintained and that the grid transitions smoothly in the far field. This can be written as

$$b_{ijk} = 3\left(\frac{s_{ijk}}{s_{ijk_{\max}}} \right)^2 - 2\left(\frac{s_{ijk}}{s_{ijk_{\max}}} \right)^3 \tag{14}$$

where k_{max} is the last node along each normal line that is allowed to deflect. Finally, the new position of each grid point can be calculated by applying the blending function to the reference, displaced grid and to the original grid:

$$\hat{x}'_{ijk} = b_{ijk}\hat{x}_{ijk} + (1 - b_{ijk})\hat{r}_{ijk} \tag{15}$$

AGARD 445.6 Wing Model

The configuration to be computed is the AGARD 445.6 weakened wing model.[16] This aeroelastic wing model is currently being used to evaluate existing methods for computing aeroelastic problems. The geometry consists of a wing with an aspect ratio, AR = 1.6525, a taper ratio of 0.6576, a quarter-chord sweepback angle of 45 deg, and a NACA 65A004 airfoil section in the streamwise direction. Experimental flutter results and a structural model for the wing using four mode shapes are presented in Ref. 16.

A series of three grids have been developed for this geometry. For each successive mesh, refinement in all three directions is performed. The finest grid cuts by half the spacing used on the coarsest grid. Details of the point distributions for each mesh are given in Table 1, where i is around the body, j is in the spanwise direction, and k is normal to the body. The grids are of C–H type, and Fig. 1 shows a view of the wing surface geometry. The grid extended eight root chord lengths downstream of the trailing edge, six root chords to the upper, lower, and upstream boundaries, and one semispan from the tip.

Reference 16 provided a structural model for the AGARD 445.6 wing that consisted of the first four natural vibration modes. In a recent work by Kolonay,[22] a new structural model of the AGARD 445.6 wing was developed. This model contained the first 14 natural vibration modes with the first 4 modal frequencies being matched as nearly as possible to the experimental frequencies. The orthonormal mode shapes and the generalized stiffness from this model were used for the present computations. For all cases computed, it is assumed that no structural damping is present. To match the given mode shapes to the corresponding aerodynamic grids a specialized interpolation program (FASIT)[23] was employed. Both thin-plate spline and multiquadric–biharmonic interpolation methods were considered and were found to produce very similar mode shapes on the medium mesh. The thin-plate spline interpolation method is used for all subsequent results.

Table 1 Mesh distributions

	Total			Wing surface	
Grid	i	j	k	i	j
Coarse	131	41	51	91	26
Medium	197	61	75	137	39
Fine	261	81	101	181	51

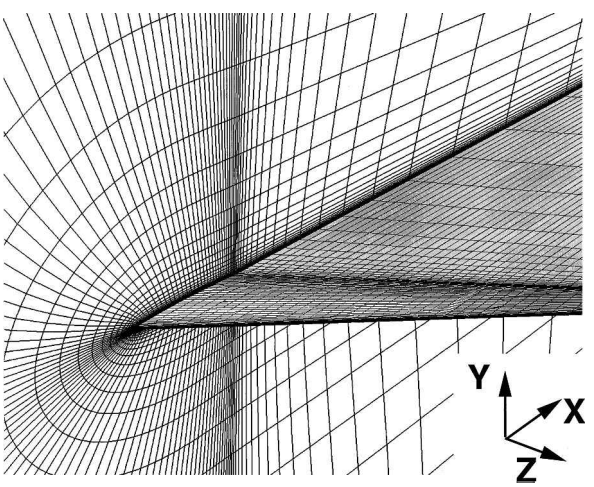

Fig. 1 C–H grid structure for the AGARD 445.6 wing.

Aerodynamic Boundary Conditions

The aerodynamic boundary conditions for the AGARD wing are as follows. At solid surfaces, the no-slip condition is applied requiring that the fluid velocity at the wing surface match the surface velocity. The remaining two conditions are the adiabatic wall condition and $\partial p/\partial n = -\rho \boldsymbol{a}_b \cdot \boldsymbol{n}$, where $\boldsymbol{a}_b$ is the acceleration of the body and $\boldsymbol{n}$ is a vector normal to the surface. A quasi-one-dimensional characteristic boundary condition was applied in the far field except at the downstream and symmetry planes, where zeroth-order extrapolation is used. In the wake regions downstream of the wing and outboard of the tip, the upper and lower wake surfaces were assigned the average of the top and bottom adjoining nodes.

Results

Dynamic computations of wing flutter are carried out for the AGARD wing for two Mach numbers, $M_\infty = 0.96$ and 1.141. Each Mach number case is run for a series of dynamic pressures to determine the flutter point. As the dynamic pressure is varied, the freestream density and Mach number are held fixed, and the Reynolds number is allowed to vary to provide a consistent set of conditions. This small variation in Reynolds number should not have a significant effect on the flow solutions.[3]

Reynolds numbers (based on the wing root chord) for the two cases are in the range from $Re = 6.145 \times 10^5$ to 6.735×10^5 for $M_\infty = 0.96$ and from $Re = 8.57 \times 10^5$ to 8.79×10^5 for $M_\infty = 1.141$. In each case the flow is assumed turbulent, and the Baldwin–Lomax[24] turbulence model is implemented to account for turbulence effects. Because no information on the location of transition is provided in the experiment, the flow is assumed to transition at the leading edge for all computations except where otherwise indicated.

A nondimensional time step $\Delta t = 0.05$ is used for all of the flutter computations. The maximum allowable time step is determined by stability considerations with the flow solver and not from the structural solver. This time step allowed for approximately 730–830 time steps per cycle of structural oscillation. All simulations are started from a steady-state, rigid, nonlifting condition. A small velocity perturbation is given to the first bending mode, and all other modes are excited from this perturbation.

$M_\infty = 0.96$

Figure 2 shows the response of the first four modes for the $M_\infty = 0.96$ case on the medium mesh for a flutter condition $q/q_e = 1.2$, where $q_e = 61.3$ lbf/ft^2 is the experimental dynamic pressure for flutter. The first bending mode appears to be the dominant mode with only the second mode showing any significant effect of the impulse applied to the first mode. The growth or decay of the first bending mode is analyzed, therefore, to determine the flutter

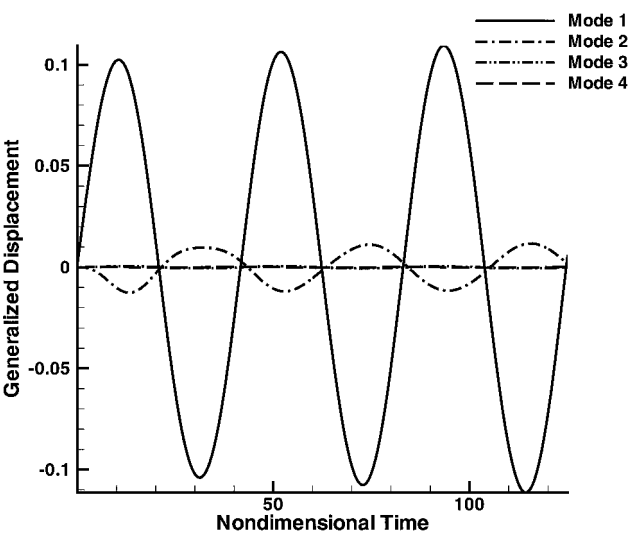

Fig. 2 Dynamic response of first four modes: $M_\infty = 0.96$ and $q/q_e = 1.2$.

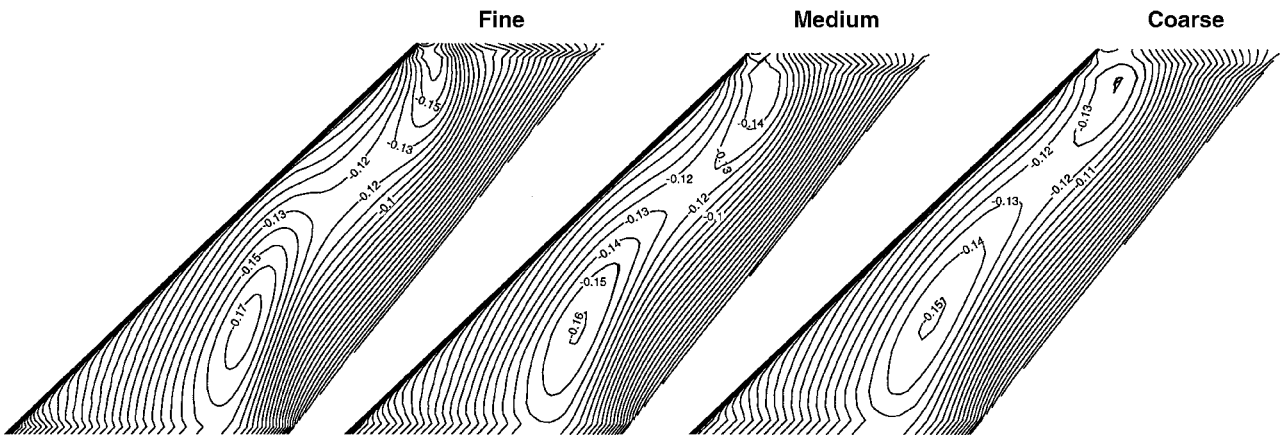

Fig. 3 Effect of grid resolution on the rigid-surface pressure coefficient, $M_\infty = 0.96$.

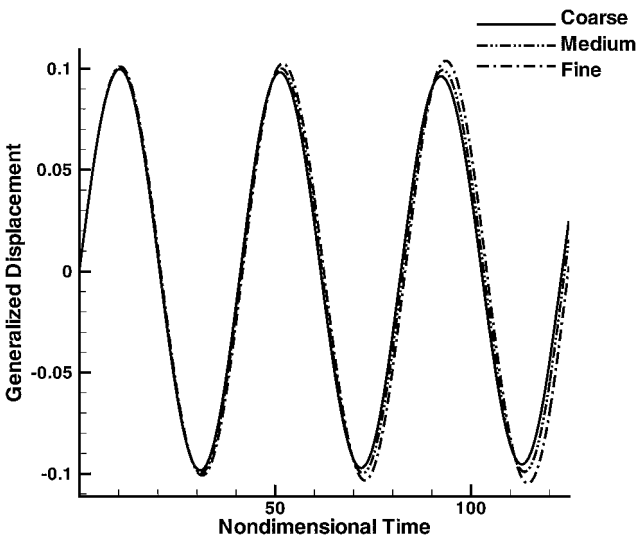

Fig. 4 Effect of grid resolution on mode 1 response: $M_\infty = 0.96$ and $q/q_e = 1.1$.

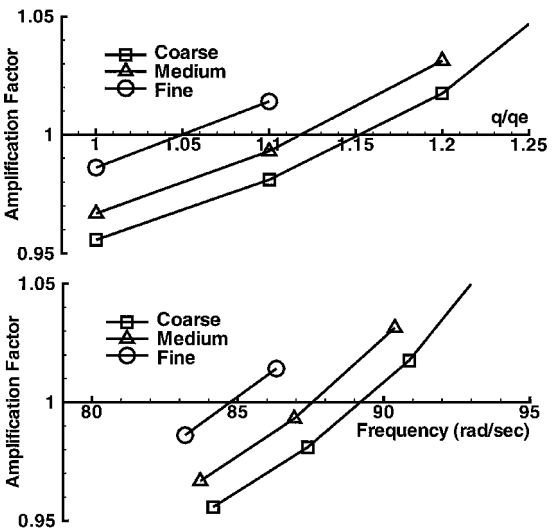

Fig. 5 Dynamic pressure and frequency for flutter, $M_\infty = 0.96$.

location. It was found by running one solution for a significantly longer period of time that only a few cycles of oscillation were required to determine whether the solution was growing or decaying for this case. This is not true for all Mach numbers, however, as will be seen in the next section.

Figure 3 demonstrates the effect of grid resolution on the computed surface pressures for $M_\infty = 0.96$. Finer mesh resolution is seen to enhance the low-pressure region over the wing. The corresponding effect of mesh resolution on the time history of the first bending mode is seen in Fig. 4 for $q/q_e = 1.1$. At this freestream dynamic pressure, the oscillations are seen to be decaying on the coarse and medium meshes and growing for the fine mesh. This indicates that the effect of improved mesh resolution is to reduce the computed flutter speed for the $M_\infty = 0.96$ case, though grid independence has not yet been achieved.

The results of all of the computations performed for $M_\infty = 0.96$ are summarized in Fig. 5. In Fig. 5, the amplification factor is defined as the ratio of the magnitude of a peak with the magnitude of the previous peak of corresponding sign. The response frequency is determined from the period between two successive peaks of the same sign. The amplification factors and response frequencies plotted in Fig. 5 are obtained from the average of the values for the last positive and negative peak. A value of amplification factor greater than 1.0 implies flutter. From Fig. 5 the effects of varying dynamic pressure q and mesh resolution can be clearly seen. As dynamic pressure is increased, the amplification factor grows and eventually exceeds 1.0, and the wing begins to flutter. Grid refinement leads to a reduction in the flutter speed and the corresponding response frequency.

The flutter points inferred from Fig. 5 are compared with other computed results[3,4] and with the experimental results[16] in Table 2. Also included in Table 2 are a corresponding set of results computed with the present scheme using the Euler equations. The flutter speed index (FSI) is defined as

$$\mathrm{FSI} = \frac{U_f}{b_s \omega_\alpha \sqrt{\bar{\mu}}} \tag{16}$$

where U_f is the flutter speed, b_s is half the root chord, ω_α is the primary torsional frequency (second mode), and $\bar{\mu}$ is the mass ratio. Note that ω/ω_α is referred to as the frequency ratio and is the ratio of the response frequency to the primary torsional frequency. The present viscous computations slightly overpredict the experimental flutter speed index and frequency ratio on the coarser meshes, but approach the experimental values with mesh refinement. The inviscid results agree well with the experimental values on the coarser meshes, but the comparison degrades with increasing mesh refinement. The solutions on all meshes, however, predict the flutter values as well as or better than the solutions in Refs. 3 and 4.

$M_\infty = 1.141$

The next case computed, $M_\infty = 1.141$, has proved much more challenging to reproduce the reported experimental flutter behavior.[3,4] This case has a shock that is located outboard, on the aft portion of the wing. The presence of the shock and the corresponding shock/boundary-layer interaction make this a more interesting flow condition to compute. Figure 6 shows the time history of the first four

modes for a dynamic pressure $q/q_e = 1.8$, where $q_e = 105.3$ lbf/ft^2. As in the $M_\infty = 0.96$ case, the first mode appears to be the dominant mode, though the higher modes appear to play more of a role for $M_\infty = 1.141$. For this case, it is also necessary to run significantly more cycles than for $M_\infty = 0.96$ before a clear determination of the response is made. In some instances, the amplitude of the first few cycles computed appeared to be growing though ultimately the solution was damped. One needs to be cautious, therefore, in trying to project a result in this situation using only a few cycles of response.

The effect of grid resolution on the surface pressure coefficient for the static initial condition is seen in Fig. 7. The most significant effect noted is a strengthening and sharpening of the shock wave on the wing. The corresponding effect on the response of the first mode is demonstrated in Fig. 8. The solution is seen to grow at a slower rate as the mesh resolution is increased implying an increase in the flutter speed. This trend is opposite from the situation for $M_\infty = 0.96$.

Figure 9 summarizes the results for the viscous computations at increasing dynamic pressures on the three meshes. Because no computation was performed for $q/q_e = 1.7$ on the fine mesh, the dashed line represents a best estimate of the shape of the curve for this grid. Figure 9 demonstrates that the effect of grid resolution is to increase the flutter speed and frequency for this case. A comparison of the computed viscous flutter values for $M_\infty = 1.141$ with the experimental values and Navier–Stokes computations of other researchers is given in Table 3. The Navier–Stokes computations are seen to overpredict the experimental flutter speed index and the frequency ratio. Note, however, that the other computations shown also overpredict the flutter point for this case. The current computations lie well within the range of computational results presented by other authors.

Computations for the $M_\infty = 1.141$ case were repeated using the Euler equations to assess viscous effects on the predicted flutter point. The Euler results are seen to give notably higher values for the flutter speed index and frequency ratio indicating a significant viscous influence on the flutter point location. This corresponds with the trend reported in Ref. 3. The computed values of FSI and frequency ratio are comparable to values reported for other Euler simulations by Lee-Rausch and Batina[3] and Farhat and Lesoinne.[25]

Table 2 Flutter point results, $M_\infty = 0.96$

Method	q/q_e	FSI	ω/ω_α
Coarse viscous	1.15	0.333	0.383
Medium viscous	1.12	0.329	0.376
Fine viscous	1.05	0.319	0.364
Coarse inviscid	1.02	0.314	0.371
Medium inviscid	0.96	0.304	0.361
Fine inviscid	0.84	0.285	0.331
Experiment[16]	1.0	0.308	0.365
Reference 3	0.89	0.294	0.346
Reference 4	1.47	0.367	0.349

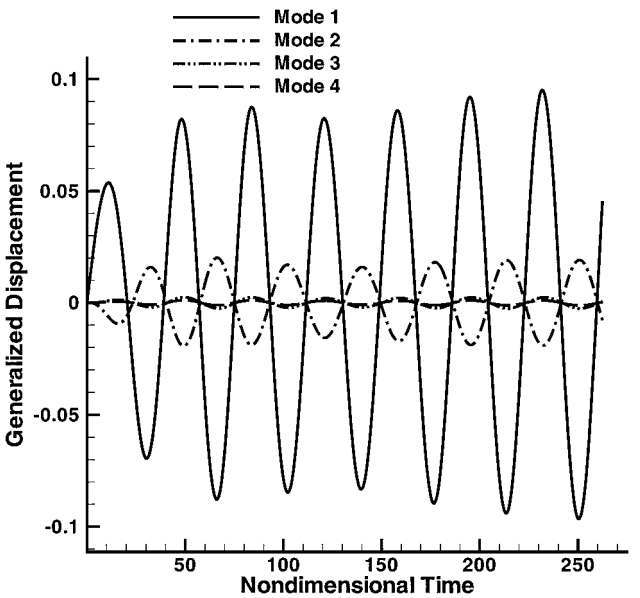

Fig. 6 Dynamic response of first four modes: $M_\infty = 1.141$ and $q/q_e = 1.8$.

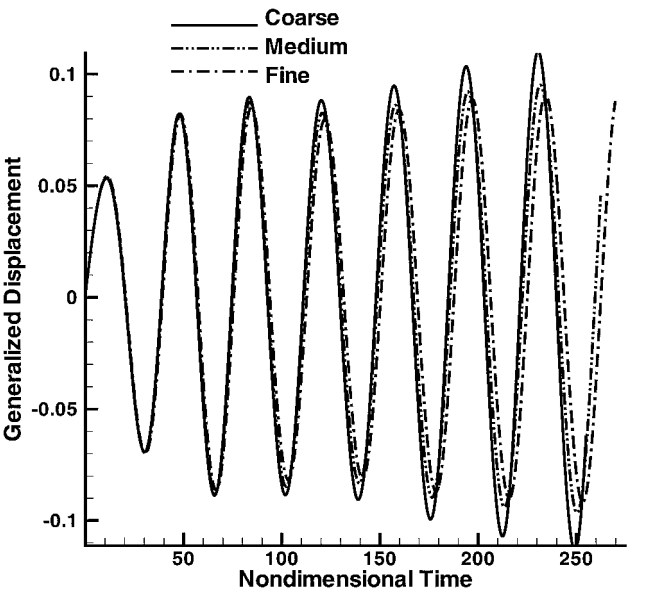

Fig. 8 Effect of grid resolution on mode 1 response: $M_\infty = 1.141$ and $q/q_e = 1.8$.

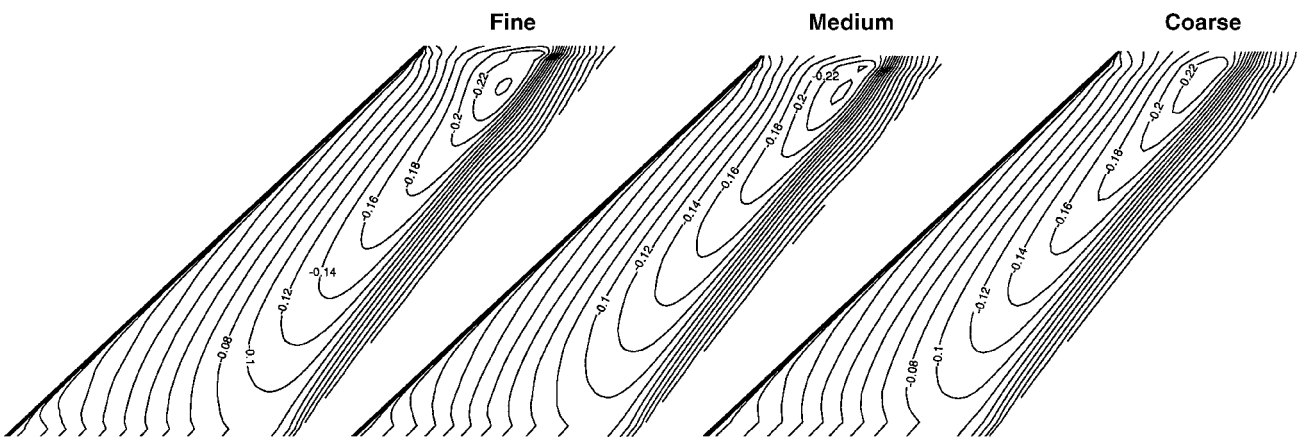

Fig. 7 Effect of grid resolution on the rigid-surface pressure coefficient, $M_\infty = 1.141$.

Table 3 Flutter point results, $M_\infty = 1.141$

Method	q/q_e	FSI	ω/ω_α
Coarse viscous	1.69	0.530	0.591
Medium viscous	1.72	0.534	0.598
Fine viscous	1.76	0.541	0.607
Coarse inviscid	2.12	0.592	0.694
Medium inviscid	2.10	0.591	0.682
Fine inviscid	2.09	0.589	0.669
Four modes	1.77	0.542	0.613
Roe	1.78	0.544	0.604
Transition 30% c	1.75	0.539	0.616
Experiment[16]	1.0	0.403	0.459
Reference 3	1.61	0.506	0.521
Reference 4	2.10	0.574	0.597

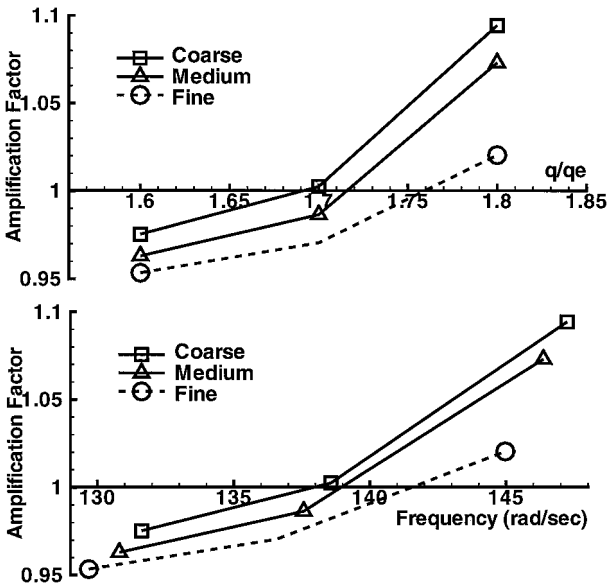

Fig. 9 Dynamic pressure and frequency for flutter, $M_\infty = 1.141$.

Gupta[26] has reported Euler simulations for which the FSI and frequency ratio predicted compare reasonably with the experimental values at the $M_\infty = 1.141$ flow condition but are underpredicted for lower values of Mach number. The trends observed in Gupta's simulations appear to be inconsistent with all of the other Euler simulations reported here.

To investigate the sensitivity of the $M_\infty = 1.141$ solution to various computational parameters, several limited studies were undertaken on the coarse mesh. Lee-Rausch and Batina[3] suggest that using a model with a higher number of modes than the four modes used in their study may be required at higher Mach numbers. As noted in Fig. 6, the higher modes show more participation in the response for the $M_\infty = 1.141$ case. The structural model used for the present computations contained 14 modes. To understand the influence of this higher mode participation, computations were carried out using only the first four modes of the model. Figure 10 shows the effect of number of modes on the response of the first mode. The reduction in the number of modes has significantly reduced the amplitude and rate of growth of the oscillations implying an increase in the flutter speed for the computations with fewer modes. This result is confirmed in Fig. 11 and Table 3, where the flutter speed and frequency are seen to be reduced with an increase in the number of modes in the model. The reduction is not significant enough, however, to explain the discrepancies between the computations and experiment. This result highlights the potential shortcomings of using highly truncated modal models in certain situations.

The present aerodynamic solver has the option of using a third-order upwind-biased Roe scheme (see Ref. 19). The effect of the improved accuracy and shock definition of this scheme on the computed results at $M_\infty = 1.141$ is also investigated. A comparison of the surface pressure coefficient for the initial condition is given in Fig. 12. A sharpening of the shock and a slight increase in the suction levels results when the Roe scheme is employed. The effect on the first mode response (Fig. 13) is to reduce the amplitude and growth rate of the oscillations. This corresponds to an increase in the flutter speed and response frequency (Fig. 14 and Table 3), which is consistent with the trend observed when the grid is refined for the central difference scheme.

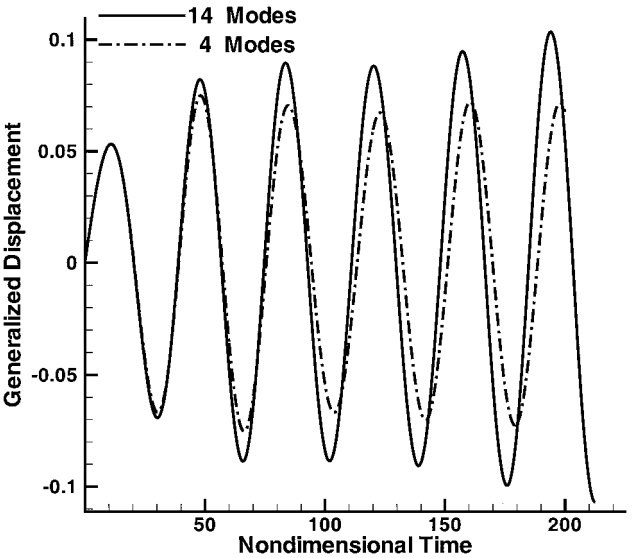

Fig. 10 Effect of number of modes used on mode 1 response: $M_\infty = 1.141$ and $q/q_e = 1.8$.

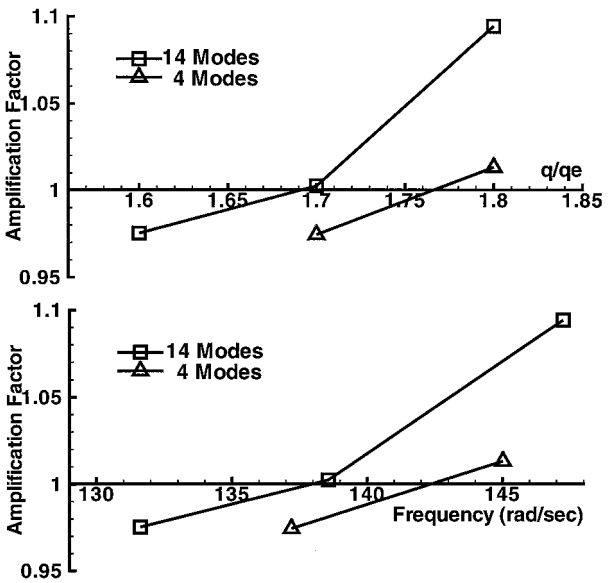

Fig. 11 Effect of number of nodes on dynamic pressure and frequency for flutter, $M_\infty = 1.141$.

Another possible source for the difference between the experiment and computation at the higher Mach number is transition. Throughout the experiments, natural boundary-layer transition was permitted. Therefore, the effect of transition location may play a role that is not being modeled in any of the computations to date. This issue has also been raised by Lee-Rausch and Batina.[3] To investigate the sensitivity of the computed flutter point to transition location, computations were performed with the Baldwin–Lomax model turned off over the first 30% of the wing. Although this may not exactly model the physical transition process that occurs, the sensitivity of the solution to transition location may be discerned. The computed results (Fig. 15 and Table 3) indicate a small increase in the flutter speed and frequency response. This effect again does not account for the discrepancy between the computations and the reported experimental results.

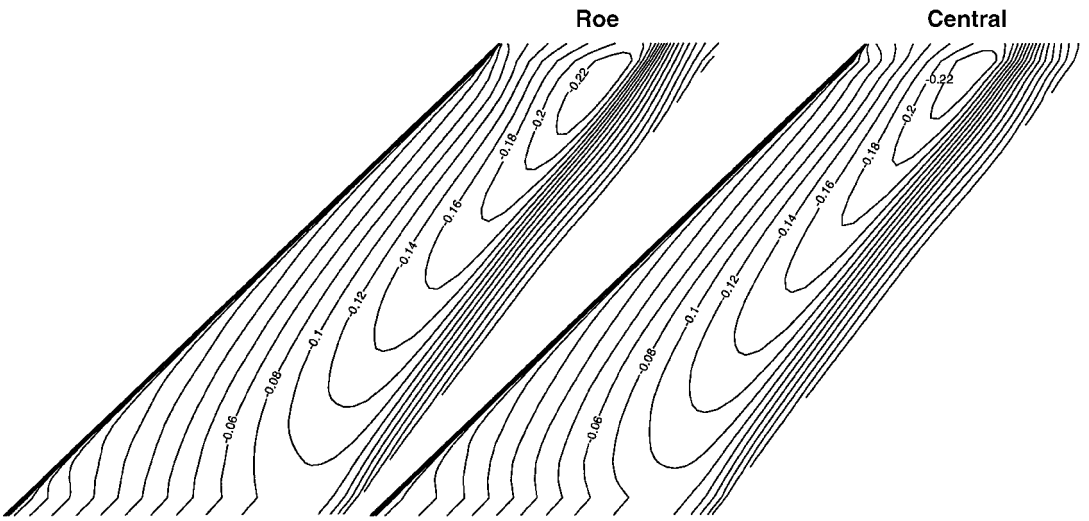

Fig. 12 Effect of Roe scheme on the rigid-surface pressure coefficient, $M_\infty = 1.141$.

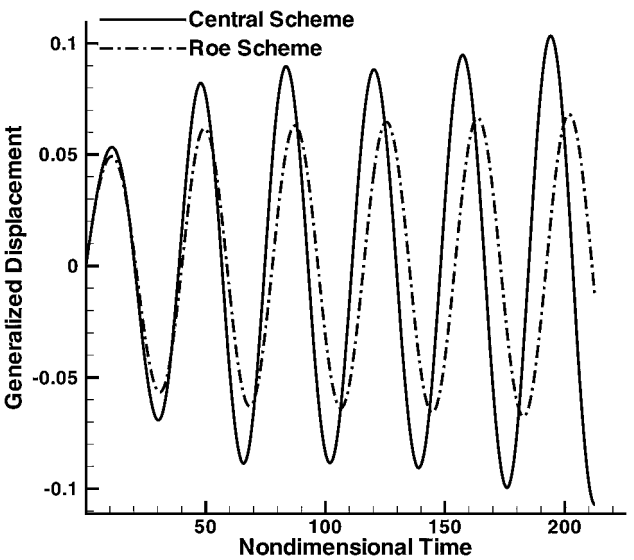

Fig. 13 Effect of Roe scheme on mode 1 response: $M_\infty = 1.141$ and $q/q_e = 1.8$.

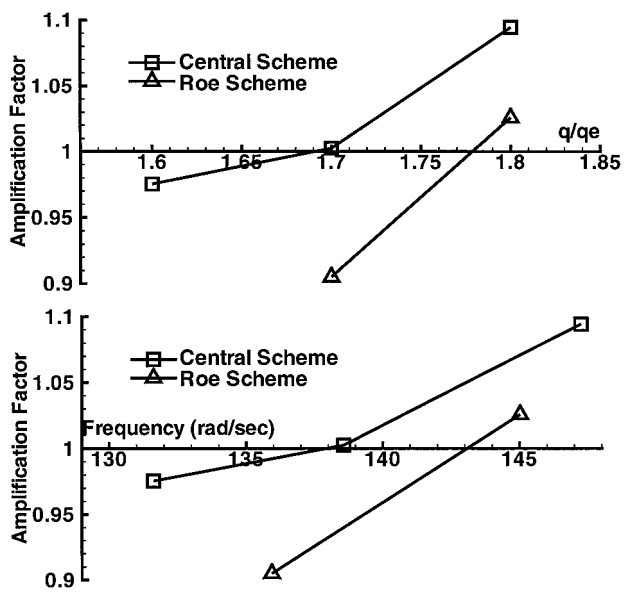

Fig. 14 Effect of Roe scheme on dynamic pressure and frequency for flutter, $M_\infty = 1.141$.

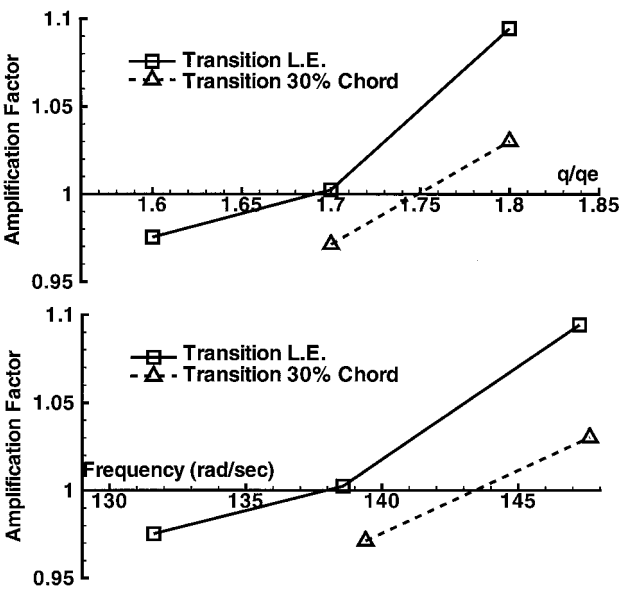

Fig. 15 Effect of transition location on dynamic pressure and frequency for flutter, $M_\infty = 1.141$.

Neither the addition of extra modes in the structural model, nor the use of the more accurate Roe scheme (or similar grid refinement), nor transition location have provided a complete resolution to the discrepancies between the experiment and computations at $M_\infty = 1.141$. Lee-Rausch and Batina[3] also investigated the effects of structural damping on the computed flow at $M_\infty = 1.141$. The small changes in the flutter speed (surprisingly in a destabilizing sense) they observed with the addition of structural damping is still not enough to account for the difference between the computations and experiment.

Further investigation is required to determine adequately the reason for the discrepancy between the experiment and computations at $M_\infty = 1.141$. Because most of the computations discussed can adequately predict the flutter characteristics at subsonic Mach numbers, it seems that the structural properties of the wing are being modeled satisfactorily. The problem, therefore, appears to be an inability to model correctly the physical processes occurring in the flutter experiment at supersonic Mach numbers. The exact cause of the problem remains difficult to determine because only minimal information on the experimental flowfield itself is available. As always with turbulent flows, the choice of turbulence model can be a key element in correctly simulating the flow. In this situation the standard Baldwin–Lomax turbulence model may be inadequate for capturing the complex physics associated

with the shock-wave/boundary-layer interaction that occurs. Alternately, the actual physical conditions in the experiment may not be properly represented in the computations. At the supersonic Mach numbers, for instance, accounting for the presence of the wind-tunnel walls may play an important role in matching the experimental flutter values. Finally, in the supersonic flow region, significant changes in flutter speed and frequency can occur for small changes in Mach number. Therefore, any small experimental error in Mach number reported could lead to significant differences between the computed and experimental flutter properties.

Conclusions

This paper has presented computations using a recently developed fully implicit, aeroelastic Navier–Stokes solver. This technique achieves implicit coupling of the fluids and structures via a subiteration strategy. Flutter computations on the AGARD 445.6 standard aeroelastic wing were performed for two Mach numbers, $M_\infty = 0.96$ and 1.141.

For the $M_\infty = 0.96$ case, the present viscous computations predict the flutter point well for all grids considered. The effect of improved grid resolution is to reduce the flutter speed providing better agreement between experiment and computation. Computations using an Euler solver compared well on the coarser meshes, but the comparison degraded with mesh refinement.

The $M_\infty = 1.141$ case has a shock located outboard on the aft portion of the wing. Whereas the present viscous computations significantly overpredict the experimental flutter point for this case, the computations are consistent with other computational results presented for the same case. Computations for the present paper were performed on grids significantly finer than previous works. The effect of grid refinement on the viscous solutions was to increase the flutter speed slightly. Euler computations for the $M_\infty = 1.141$ case showed significant differences from the viscous solutions. The flutter speeds and frequency response were higher than the viscous values and further from the reported experimental values. Viscous effects are clearly playing an important role in this case.

Solutions for this case were also obtained using both 4 and 14 modes in the structural model. Although increasing the number of modes in the structural model reduces the predicted flutter speed at this Mach number, the reduction is not enough to account for the discrepancies between the computations and experiment. The computations were repeated using a third-order, upwind-biased Roe scheme. The trends observed using the Roe scheme were consistent with those observed when grid refinement was performed. Finally, the location of the computational transition location was moved downstream from the leading edge to the 30% chord location. Only a minimal effect of this change was observed in the flutter response.

Acknowledgments

The work presented was sponsored by the U.S. Air Force Office of Scientific Research under Task 2304/IN, monitored by L. Sakell. Computational resources were provided by the Department of Defence High Performance Computing Major Shared Resource Centers at the U.S. Army Engineer Research and Development Center and the Naval Oceanographic Office. The authors wish to thank Ray Kolonay for providing the AGARD 445.6 wing model and Joel Luker for assisting with the use of FASIT. Many useful discussions with Scott Morton are also gratefully acknowledged.

References

[1]Guruswamy, G. P., "Unsteady Aerodynamic and Aeroelastic Calculations for Wings Using Euler Equations," *AIAA Journal*, Vol. 28, No. 3, 1990, pp. 461–469.

[2]Alonso, J., Martinelli, L., and Jameson, A., "Multigrid Unsteady Navier–Stokes Calculations with Aeroelastic Applications," AIAA Paper 95-0048, Jan. 1995.

[3]Lee-Rausch, E. M., and Batina, J. T., "Wing Flutter Computations Using an Aerodynamic Model Based on the Navier–Stokes Equations," *Journal of Aircraft*, Vol. 33, No. 6, 1996, pp. 1139–1147.

[4]Vermeersch, S. A., Weed, R. A., Sankar, L. N., and Raj, P., "Towards Cost-Effective Aeroelastic Analysis on Advanced Parallel Computing Systems," AIAA Paper 97-0646, Jan. 1997.

[5]Smith, M. J., "Flight Loads Prediction Methods for Aircraft: Vol. I. Euler/Navier–Stokes Aeroelastic Method (ENS3DAE) Technical Development Summary: Version 4.0," Supersedes WRDC-TR-89-3104 (to be published), Nov. 1989.

[6]Paneer, R., Visbal, M. R., and Morton, S. A., "Computation of Nonlinear Panel Flutter Using a Fully Implicit Aeroelastic Solver," AIAA Paper 98-1844, April 1998.

[7]Melville, R. B., Morton, S. A., and Rizzetta, D. P., "Implementation of a Fully-Implicit, Aeroelastic Navier–Stokes Solver," AIAA Paper 97-2039, June 1997.

[8]Beam, R. M., and Warming, R. F., "An Implicit Factored Scheme for the Compressible Navier–Stokes Equations," *AIAA Journal*, Vol. 16, No. 4, 1978, pp. 393–402.

[9]Visbal, M. R., "Onset of Vortex Breakdown Above a Pitching Delta Wing," *AIAA Journal*, Vol. 32, No. 8, 1994, pp. 1568–1575.

[10]Gordnier, R. E., "Computation of Delta Wing Roll Maneuvers," *Journal of Aircraft*, Vol. 32, No. 3, 1995, pp. 486–492.

[11]Visbal, M. R., "Numerical Simulation of Spiral Vortex Breakdown Above a Delta Wing," AIAA Paper 95-2309, June 1995.

[12]Gordnier, R. E., and Visbal, M. R., "Numerical Simulation of the Impingement of a Streamwise Vortex on a Plate," AIAA Paper 97-1781, June 1997.

[13]Morton, S. A., Melville, R. B., and Visbal, M. R., "Accuracy and Coupling Issues of Aeroelastic Navier–Stokes Solutions on Deforming Meshes," AIAA Paper 97-1085, April 1997.

[14]Thomas, P. D., and Lombard, C. K., "Geometric Conservation Law and Its Application to Flow Computations on Moving Grids," *AIAA Journal*, Vol. 17, No. 10, 1979, pp. 1030–1037.

[15]Melville, R. B., and Morton, S. A., "Fully Implicit Aeroelasticity on Overset Grid Systems," AIAA Paper 98-0521, Jan. 1998.

[16]Yates, E. C., Jr., "AGARD Standard Aeroelastic Configurations for Dynamic Response I.—Wing," AGARD-R-765, July 1988.

[17]Pulliam, T. H., and Steger, J. L., "Implicit Finite-Difference Simulation of Three-Dimensional Compressible Flows," *AIAA Journal*, Vol. 18, No. 2, 1980, pp. 159–167.

[18]Gordnier, R. E., and Visbal, M. R., "Numerical Simulation of the Unsteady Vortex Structure over a Delta Wing," AIAA Paper 91-1811, June 1991.

[19]Gaitonde, D., Edwards, J. R., and Shang, J. S., "The Computed Structure of a 3-D Turbulent Interaction Caused by a Cylinder/Offset Flare Juncture," AIAA Paper 95-0230, 1995.

[20]Pulliam, T. H., and Chaussee, D. S., "A Diagonal Form of an Implicit Approximate-Factorization Algorithm," *Journal of Computational Physics*, Vol. 39, No. 2, 1981, pp. 347–363.

[21]Jameson, A., Schmidt, W., and Turkel, E., "Numerical Solutions of the Euler Equations by Finite Volume Methods Using Runge–Kutta Time-Stepping Schemes," AIAA Paper 81-1259, 1981.

[22]Kolonay, R. M., "Unsteady Aeroelastic Optimization in the Transonic Regime," Ph.D. Dissertation, Dept. of Aeronautics and Astronautics, Purdue Univ., Lafayette, IN, Dec. 1996.

[23]Smith, M. J., Hodges, D. H., and Cesnik, C. E. S., "An Evaluation of Computational Algorithms to Interface Between CFD and CSD Methodologies," WL-TR-96-3055, Air Force Research Lab., Wright–Patterson AFB, OH, Nov. 1995.

[24]Baldwin, B. S., and Lomax, H., "Thin Layer Approximation and Algebraic Model for Separated Turbulent Flow," AIAA Paper 78-0257, Jan. 1978.

[25]Farhat, C., and Lesoinne, M., "Enhanced Partitioned Procedures for Solving Nonlinear Transient Aeroelastic Problems," AIAA Paper 98-1806, April 1998.

[26]Gupta, K. K., "Development of a Finite Element Aeroelastic Analysis Capability," *Journal of Aircraft*, Vol. 33, No. 5, 1996, pp. 995–1002.